

# Ab Initio Molecular Dynamics with Discrete Variable Representation Basis Sets: Techniques and Application to Liquid Water<sup>†</sup>

Hee-Seung Lee

Department of Chemistry, New York University, New York, New York 10003

Mark E. Tuckerman\*

Department of Chemistry and Courant Institute of Mathematical Sciences, New York University, New York, New York 10003

Received: December 5, 2005; In Final Form: February 23, 2006

Finite temperature ab initio molecular dynamics (AIMD), in which forces are obtained from “on-the-fly” electronic structure calculations, is a widely used technique for studying structural and dynamical properties of chemically active systems. Recently, we introduced an AIMD scheme based on discrete variable representation (DVR) basis sets, which was shown to have improved convergence properties over the conventional plane wave (PW) basis set [Liu, Y.; et al. *Phys. Rev. B* **2003**, 68, 125110]. In the present work, the numerical algorithms for the DVR based AIMD scheme (DVR/AIMD) are provided in detail, and the latest developments of the approach are presented. The accuracy and stability of the current implementation of the DVR/AIMD scheme are tested by performing a simulation of liquid water at ambient conditions. The structural information obtained from the present work is in good agreement with the result of recent AIMD simulations with a PW basis set (PW/AIMD). Advantages of using the DVR/AIMD scheme over the PW/AIMD method are discussed. In particular, it is shown that a DVR/AIMD simulation of liquid water in the complete basis set limit is possible with a relatively small number of grid points.

## I. Introduction

Over the last two decades, substantial theoretical and algorithmic advances in the area of ab initio molecular dynamics (AIMD) simulations have been made.<sup>1–4</sup> These methods, which employ a density functional theory (DFT) representation of the electronic structure, are now routinely used to interpret experimental data and predict the properties of a wide variety of materials. A widely used AIMD technique is the Car–Parrinello ab initio molecular dynamics (CPAIMD) based on the extended Lagrangian approach and, in most implementations, a plane-wave (PW) expansion of the electronic orbitals.<sup>5</sup> The efficiency of CPAIMD comes from the fictitious dynamics of the orbitals that allow “on the fly” generation of the interatomic forces. Although the PW basis is conceptually simple and widely used for periodic systems, it has one critical disadvantage: PW based algorithms scale as  $\mathcal{O}(N^2M)$ , where  $N$  is the number of occupied electronic states and  $M$  is the number of basis functions. This bottleneck currently limits the application of CPAIMD up to a few hundred atoms. In addition, PW based methods rely heavily on the use of fast Fourier transform (FFT), and this reliance is not optimal for massively parallel computers due to the need for global (all-to-all type) communications among processors.

To overcome these difficulties, many alternatives have been introduced, including novel parallelization schemes,<sup>68</sup> Gaussian basis sets,<sup>6,7</sup> hybrid Gaussian/PW basis sets<sup>8</sup> and real-space approaches.<sup>9–13</sup> Some of these alternative methods have attracted increasing interest in recent years for the development of linear scaling ( $\mathcal{O}(N)$ ) electronic structure calculations.<sup>14–18</sup> Real-space methods, such as finite difference<sup>19</sup> and finite element,<sup>20</sup> do not

have associated basis functions because the electronic orbitals are discretized on a 3-dimensional (3D) grid. However, an advantage of real-space methods is that they are inherently local and can be efficiently implemented on massively parallel computers. The Hamiltonian matrix is very sparse, and efficient matrix–vector multiplication algorithms can be used to obtain the Kohn–Sham orbitals. In addition, when real-space methods are combined with an orbital localization scheme, the result is a method that can be made to scale linearly with respect to the system size.<sup>11</sup> In fact, a large scale ( $\sim 1000$  atoms) electronic structure calculation was performed with a real-space method and showed that  $\mathcal{O}(N)$  scaling can be achieved in practice.<sup>21</sup>

The numerical methods to solve the Kohn–Sham equation on a real-space grid have been pioneered by Beck,<sup>12</sup> Bernholc,<sup>10</sup> and Chelikowsky.<sup>19</sup> In the usual implementation of real-space methods, gradient and Laplacian operators are discretized on the grid and a high order finite difference scheme is used to approximate the kinetic energy operator. Potential energies, which involve the overlap integrals between the electronic orbitals and the atomic pseudopotentials, are evaluated directly on the grid by summing the values of integrand over the grid points. However, the Hartree potential cannot be computed directly on the grid because it leads to a prohibitively expensive double summation over the grid points. Instead, the Hartree potential is obtained by iteratively solving the Poisson equation with the proper boundary condition. Because the Kohn–Sham equation is a nonlinear equation that requires iterative updates of solutions, each update step involves an iterative solution of the Poisson equation. Various types of multigrid methods<sup>22,23</sup> have been developed to accelerate the convergence of the iterative solutions of both the Kohn–Sham equation and the

<sup>†</sup> Part of the special issue “John C. Light Festschrift”.

Poisson equation. For more technical details of multigrid methods and their applications to the solutions of the Kohn–Sham equation as well as linear scaling electronic structure calculations, readers are referred to the review by Beck.<sup>12</sup>

Although  $\mathcal{O}(N)$  scaling electronic structure calculations have been actively pursued, only a limited number of AIMD studies with real-space methods have been reported.<sup>10,24–26</sup> In fact, to the best of our knowledge, the most complicated *condensed phase* system that has been successfully simulated so far with a real-space method is a liquid silicon system.<sup>24</sup> No real-space method has yet been applied to study aqueous systems. Furthermore, most real-space AIMD methods are based on the so-called Born–Oppenheimer *ab initio* molecular dynamics (BOAIMD) scheme, where the electronic wavefunctions are explicitly quenched to the ground state at each AIMD step. Although a larger time step can be used in BOAIMD simulations than in CPAIMD simulations, it is a well-known fact that the BOAIMD scheme requires a very strict convergence criterion for minimization of the Kohn–Sham functional at each time step to avoid substantial drifts in the conserved energy. The question of the relative efficiency of CPAIMD vs BOAIMD is still being debated in the literature.<sup>3,27</sup> To develop an efficient linear scaling AIMD method, we choose to develop an accurate and stable scheme based on real-space methods within the CPAIMD framework. However, due to the extreme sensitivity of CPAIMD simulations to the continuity and accuracy of the force evaluations, difficulties may arise when typical grid-based methods are applied to the CPAIMD scheme. Even a small random error can jeopardize the long-term stability of CPAIMD simulations.

Recently, we developed a discrete variable representation (DVR) approach<sup>28,29</sup> for CPAIMD simulations as an alternative real-space method for the implementation of AIMD calculations on massively parallel computers.<sup>30</sup> DVRs have been extensively used in the nuclear quantum dynamics community for decades but it is a new approach for electronic structure calculations and AIMD simulations. Unlike conventional real-space methods, a DVR is a *basis set* approach, and the kinetic energy is evaluated *exactly* for the specified basis set. DVR basis functions are localized in space but defined *everywhere*, not just on grid points. Consequently, they do not employ explicit spatial cutoffs. As in a plane-wave basis set, the orbitals are represented by a set of expansion coefficients. However, in a DVR, a one-to-one correspondence exists between coefficients and grid points. Moreover, the independence of the basis functions on the atomic positions makes the calculation of atomic forces easier to evaluate than in a basis of atom-centered basis functions such as Gaussians. In our previous publication,<sup>30</sup> we demonstrated the advantage of DVR basis sets over PW basis sets in terms of the energy cutoff required to converge the total energy of solid silicon and a single water molecule. We also showed the stability of CPAIMD simulations with DVRs by performing a short (2 ps) simulation of solid silicon system.

In the present work, we describe the newest developments of the original approach and apply the current implementation of the DVR based CPAIMD scheme (DVR/CPAIMD) to simulate a liquid water system that consists of 32 water molecules in a periodic box. To obtain accurate results for the liquid water system, a simulation of at least 20 ps or more is necessary. In addition, the highly repulsive oxygen pseudopotential makes it difficult to perform an accurate and efficient CPAIMD simulation of liquid water with any real-space method. Therefore, the liquid water system serves as an important benchmark to test rigorously the accuracy and stability of the

DVR/CPAIMD scheme. Here, we present preliminary results of our simulation of liquid water and focus on the accuracy and stability of the DVR/CPAIMD scheme with the BLYP<sup>31,32</sup> exchange–correlation functional. With the grid spacing used in this work, the total energy of a 32 water system is converged to within  $10^{-3}$  hartree, whereas the typical 70 Ry energy cutoff in PW calculations leads to a total energy more than 1 hartree from the converged value. Therefore, a DVR basis allows us to perform a CPAIMD simulation of liquid water at ambient conditions *at or near the complete basis set limit*. Given the fact that recent AIMD studies of water,<sup>33–41</sup> all based on PW or hybrid Gaussian/PW basis sets, showed a wide range of structural parameters, depending on the basis set, equilibration method, exchange–correlation functional, and type of ensemble, the results obtained from DVR/CPAIMD simulations that accurately describe the electronic structure of water can shed light on the accuracy of CPAIMD simulations for a given density functional.

The organization of this paper is as follows. In section II, the basic properties of DVR bases are briefly described. Following this, a succinct description of the current implementation of the DVR/CPAIMD scheme is presented in section III with particular attention given to the nonlocal part of the pseudopotential calculation. In section IV, the accuracy and improved efficiency of total energy calculations are discussed as well as the preconditioner used in the energy minimization procedure. This will be followed by preliminary results of a liquid water simulation under constant volume and temperature conditions. Conclusions and future work are given in section V.

## II. Discrete Variable Representation (DVR)

The definition and properties of DVRs are well documented in the literature.<sup>28,29</sup> In this section, we only provide the basic concepts that are relevant to our application of the DVR method to CPAIMD simulations. There are several equivalent ways to define a DVR, for example, using classical orthogonal polynomials (Chebyshev, Hermite, ...) and an associated Gaussian quadrature. However, all that is required is the specification of a set of functions  $\{C_l(x)\}$  that satisfy an orthogonality relation with respect to an appropriate weight function  $\omega(x)$ :

$$\int_a^b \omega(x) C_l^*(x) C_m(x) dx = \delta_{lm} \quad (1)$$

If we define our basis functions (often called a finite basis representation, (FBR)) as  $\phi_l(x) = \sqrt{\omega(x)}C_l(x)$ , the overlap integrals can be evaluated *exactly* with  $N$ -point Gaussian quadrature for  $0 \leq l, m \leq N - 1$ :

$$\begin{aligned} \int_a^b \phi_l^*(x) \phi_m(x) dx &= \sum_{\alpha=1}^N \frac{\omega_\alpha}{\omega(x_\alpha)} \phi_l^*(x_\alpha) \phi_m(x_\alpha) \\ &= \sum_{\alpha=1}^N \omega_\alpha C_l^*(x_\alpha) C_m(x_\alpha) \\ &= \delta_{lm} \end{aligned} \quad (2)$$

where  $\{x_\alpha\}$  is a set of Gaussian quadrature points and  $\{\omega_\alpha\}$  are the corresponding quadrature weights. Because  $N$ -point Gaussian quadrature is exact for integrands up to order  $2N - 1$ , the

coordinate matrix for basis functions  $\{\phi_l(x)\}$  can be evaluated exactly with the same quadrature:

$$\begin{aligned} \mathbf{X}_{lm} &= \int_a^b \phi_l^*(x) x \phi_m(x) dx \\ &= \sum_{\alpha=1}^N \frac{\omega_{\alpha}}{\omega(x_{\alpha})} \phi_l^*(x_{\alpha}) x_{\alpha} \phi_m(x_{\alpha}) \end{aligned} \quad (3)$$

From eq 3, the elements of the “transformation matrix” is defined as

$$\mathbf{T}_{\alpha l} = \sqrt{\frac{\omega_{\alpha}}{\omega(x_{\alpha})}} \phi_l(x_{\alpha}) \quad (4)$$

and the coordinate matrix in a DVR is formally defined through the transformation matrix as

$$\mathbf{X} = \mathbf{T}^{\dagger} \mathbf{X}^{\text{DVR}} \mathbf{T} \quad (5)$$

where  $\mathbf{X}^{\text{DVR}}$  is a diagonal matrix whose elements are the “DVR points”,  $\{x_{\alpha}\}$ . Note that the matrix  $\mathbf{T}$  is unitary due to eq 2. The transformation matrix defined in eq 4 leads to the formal definition of the DVR basis functions,  $\{u_{\alpha}(x)\}$ , corresponding to the DVR points  $\{x_{\alpha}\}$ :

$$u_{\alpha}(x) = \sum_{l=1}^N \mathbf{T}_{l\alpha}^{\dagger} \phi_l(x) \quad (6)$$

As is clear from the definition, eq 6, DVR functions are continuous and defined everywhere in space. One of the most important properties of a DVR function is that the values of  $u_{\alpha}(x)$  are zero at all DVR points except  $x_{\alpha}$ : i.e.

$$\begin{aligned} u_{\alpha}(x_{\beta}) &= \sum_{l=1}^N \mathbf{T}_{l\alpha}^{\dagger} \phi_l(x_{\beta}) \\ &= \sqrt{\frac{\omega(x_{\beta})}{\omega_{\beta}}} \delta_{\alpha\beta} \end{aligned} \quad (7)$$

To obtain the second equality in eq 7, the fact that the  $\mathbf{T}$  matrix is unitary was used. With the above definition of the DVR functions, the overlap integrals for the DVR functions are also equal to the Kronecker delta (cf. eq 2)

$$\begin{aligned} \int_a^b u_{\alpha}(x) u_{\beta}(x) dx &= \sum_{\gamma=1}^N \frac{\omega_{\gamma}}{\omega(x_{\gamma})} u_{\alpha}(x_{\gamma}) u_{\beta}(x_{\gamma}) \\ &= \sum_{\gamma=1}^N \frac{\omega_{\gamma}}{\omega(x_{\gamma})} \sqrt{\frac{\omega(x_{\gamma})}{\omega_{\gamma}}} \delta_{\alpha\gamma} \sqrt{\frac{\omega(x_{\gamma})}{\omega_{\gamma}}} \delta_{\beta\gamma} \\ &= \delta_{\alpha\beta} \end{aligned} \quad (8)$$

The choice of FBR functions is usually determined by the boundary conditions of the problem. In many condensed-phase applications, the system is confined in a three-dimensional periodic box. In these cases, the DVR functions can be constructed from plane-wave-like functions (or Chebyshev polynomials), and the one-dimensional (1D) FBR functions  $\{\phi_l(x)\}$  can be defined in  $[-L/2, L/2]$  as

$$\phi_l(x) = \frac{1}{\sqrt{L}} e^{2\pi i k_l x / L} \quad k_l = -N, -N+1, \dots, N \quad (9)$$

for  $l = 1, 2, \dots, 2N+1$ , where  $L$  is the box length and the number of basis functions is  $2N+1$ . For periodic functions, an equally spaced grid ensures the accuracy of the Gaussian quadrature (or Gauss-Chebyshev quadrature of the first kind), and the DVR points are given by

$$x_{\alpha} = \frac{L}{2N+1} (\alpha - N - 1) \quad \alpha = 1, 2, \dots, 2N+1 \quad (10)$$

and the elements of transformation matrix become

$$\mathbf{T}_{\alpha l} = \frac{1}{\sqrt{2N+1}} e^{2\pi i k_l x_{\alpha} / L} \quad (11)$$

Hence, for a one-dimensional periodic system, a DVR function can be defined explicitly as

$$u_{\alpha}(x) = \sum_{l=1}^{2N+1} \sqrt{\frac{1}{L(2N+1)}} \cos\left[\frac{2\pi k_l (x - x_{\alpha})}{L}\right] \quad (12)$$

Note that  $\omega(x) = 1$  and  $\omega_{\alpha} = L/(2N+1)$  for an equally spaced grid. Finally, for the system with three-dimensional periodic boundary conditions, a direct product of one-dimensional DVR functions for each coordinate,

$$\Phi_{\alpha\beta\gamma}(\mathbf{r}) = u_{\alpha}(x) u_{\beta}(y) u_{\gamma}(z) \quad (13)$$

can be used to define a three-dimensional DVR for a simple cubic box. Extensions to noncubic boxes is straightforward.

### III. Car–Parrinello Molecular Dynamics with DVR

The Car–Parrinello AIMD scheme is based on an extended system Lagrangian, which describes the dynamics of  $N$  nuclei and introduces a fictitious adiabatic dynamics of  $N_s$  orbitals as a means of propagating the optimized electronic structure from one nuclear configuration to the next without explicit minimization. The Lagrangian is given by

$$\begin{aligned} \mathcal{L} = & \mu \sum_{i=1}^{N_s} \langle \dot{\psi}_i | \dot{\psi}_i \rangle + \frac{1}{2} \sum_{I=1}^N M_I \dot{\mathbf{R}}_I^2 - E[\{\psi_i\}, \{\mathbf{R}_I\}] + \\ & \sum_{ij} \Lambda_{ij} (\langle \psi_i | \psi_j \rangle - \delta_{ij}) \end{aligned} \quad (14)$$

where  $\mu$  is a time-scale parameter associated with the fictitious orbital dynamics,  $M_I$  and  $\mathbf{R}_I$  are the mass and the position of atom  $I$  and  $\{\Lambda_{ij}\}$  is a set of Lagrange multipliers that impose the orthonormality of the orbitals. The atoms and orbitals are propagated simultaneously via an adiabatic dynamics scheme in which the orbitals are kept “cold” compared to the nuclei, such that the electronic orbitals closely follow the instantaneous Born–Oppenheimer ground-state surface. The electronic energy,  $E$ , which serves as the potential energy for the atoms in the system, is usually computed by using density functional theory (DFT). In the Kohn–Sham formulation of DFT, the energy functional is given by

$$\begin{aligned} E[\{\psi_i\}, \{\mathbf{R}_I\}] = & T_s[\{\psi_i\}] + E_{\text{H}}[n] + E_{\text{xc}}[n] + E_{\text{N}}(\{\mathbf{R}_I\}) + \\ & E_{\text{ext}}[n; \{\mathbf{R}_I\}] \end{aligned} \quad (15)$$

where  $n(\mathbf{r}) = \sum_i f_i |\psi_i(\mathbf{r})|^2$  is the electron density,  $f_i$  is the occupation number of the  $i$ th orbital,  $T_s$  is the kinetic energy of the Kohn–Sham noninteracting electron system,  $E_{\text{H}}$  is the Hartree energy,  $E_{\text{xc}}$  is the exchange–correlation energy and  $E_{\text{N}}$  is the electrostatic interaction between the atoms.

In the present DVR based DFT scheme, the Kohn–Sham orbitals are expanded in terms of direct products of one-dimensional DVR functions, eq 13, such that

$$\psi_i(\mathbf{r}) = \sum_{\alpha\beta\gamma} C_{\alpha\beta\gamma}^i \Phi_{\alpha\beta\gamma}(\mathbf{r}) \quad (16)$$

where  $\{C_{\alpha\beta\gamma}^i\}$  is a set of expansion coefficients for the state  $i$ . A DVR expansion of the orbitals leads to the density expression,

$$n(\mathbf{r}) = \sum_i f_i \left| \sum_{\alpha\beta\gamma} C_{\alpha\beta\gamma}^i \Phi_{\alpha\beta\gamma}(\mathbf{r}) \right|^2 \quad (17)$$

and the density at a DVR point is simply given by

$$\begin{aligned} n(\mathbf{r}_{\alpha''\beta''\gamma''}) &= \\ & \sum_i f_i \sum_{\alpha\beta\gamma} C_{\alpha\beta\gamma}^i \Phi_{\alpha\beta\gamma}(\mathbf{r}_{\alpha''\beta''\gamma''}) \sum_{\alpha'\beta'\gamma'} C_{\alpha'\beta'\gamma'}^i \Phi_{\alpha'\beta'\gamma'}(\mathbf{r}_{\alpha''\beta''\gamma''}) \quad (18) \\ &= \sum_i f_i |C_{\alpha''\beta''\gamma''}^i|^2 \quad (19) \end{aligned}$$

It should be noted that, unlike conventional real-space methods, the electronic orbitals and density expressed in terms of DVR functions are defined everywhere in space and each term in the energy functional has a well-defined expression. In the following, we describe the energy and force expressions for each term that appears in the energy functional of eq 15 within the DVR formalism as well as the current implementation of the method in the PINY\_MD code.<sup>42</sup> For simplicity, we assume that the number of grid points along each coordinate is the same, but the extension to a noncubic grid is straightforward. For a cubic grid, only the grid spacing,  $h$ , controls the accuracy of the total energy calculation. Note that a grid spacing  $h$  is equivalent to an energy cutoff  $\pi^2/h^2$  Ry in plane-wave calculations. If a single grid is used to represent both the orbitals and the density, as done here, then  $h$  is required to be small enough to describe the spatial fluctuations of the density. In this case,  $\pi^2/h^2$  would correspond to the energy cutoff of a density expansion in a PW basis. However, one could also imagine using a grid spacing of  $2h$  to describe the orbitals as a time-saving measure. In this case, the energy cutoff of the orbital expansion would be equivalent to  $\pi^2/4h^2$ , which leads to the expected relation between the orbital and density cutoffs in a PW basis, namely,  $E_{\text{cut}}^{(\text{dens})} = 4E_{\text{cut}}^{(\text{orb})}$ .

**(a) Kinetic Energy.** The kinetic energy, first term in eq 15, can be evaluated exactly for a given DVR basis set and the analytical expressions of the kinetic energy matrix elements for our one-dimensional DVR functions, eq 12, are available.<sup>43</sup> The full kinetic energy matrix,  $K_{\alpha\beta\gamma}^{\alpha'\beta'\gamma'}$ , is then constructed by a direct product of three one-dimensional kinetic energy matrices for each coordinate, and the kinetic energy is obtained by

$$-\frac{1}{2} \sum_i f_i \langle \psi_i | \nabla^2 | \psi_i \rangle = \sum_i f_i \sum_{\alpha\alpha'} \sum_{\beta\beta'} \sum_{\gamma\gamma'} C_{\alpha\beta\gamma}^i K_{\alpha\beta\gamma}^{\alpha'\beta'\gamma'} C_{\alpha'\beta'\gamma'}^i \quad (20)$$

The force on the orbital coefficient  $C_{\alpha\beta\gamma}^i$  is therefore given by

$$F_{\alpha\beta\gamma}^i = -2f_i \sum_{\alpha'} \sum_{\beta'} \sum_{\gamma'} K_{\alpha\beta\gamma}^{\alpha'\beta'\gamma'} C_{\alpha'\beta'\gamma'}^i \quad (21)$$

For example, for the FBR of eq 9, the matrix  $K_{\alpha\beta\gamma}^{\alpha'\beta'\gamma'}$  is given by

$$K_{\alpha\beta\gamma}^{\alpha'\beta'\gamma'} = t_{\alpha\alpha'} \delta_{\beta\beta'} \delta_{\gamma\gamma'} + t_{\beta\beta'} \delta_{\alpha\alpha'} \delta_{\gamma\gamma'} + t_{\gamma\gamma'} \delta_{\alpha\alpha'} \delta_{\beta\beta'} \quad (22)$$

where

$$t_{mm'} = -\left(\frac{2\pi}{L}\right)^2 \frac{N(N+1)\delta_{mm'}}{6} - \frac{\left(\frac{2\pi}{L}\right)^2 (-1)^{n-n'} \cos\left[\frac{\pi(n-n')}{N_g}\right]}{4 \sin^2\left[\frac{\pi(n-n')}{N_g}\right]} (1 - \delta_{mm'}) \quad (23)$$

where  $N_g = 2N + 1$  is the number of grid points and  $L$  is the length of the box in a given direction. Efficient implementation of the kinetic energy in a DVR basis requires transposition of the orbital coefficient matrix so that, for each spatial direction, summations are performed over an index that is contiguous in memory. This operation requires an all-to-all communication step. We note that although it is not possible to truncate the primitive kinetic energy matrix,  $t_{mm'}$ , improved efficiency in the calculation of the total kinetic energy is expected when localized orbitals are used.

**(b) Hartree Energy.** In the DVR approach, the Hartree energy and coefficient forces are computed in reciprocal space because the Hartree energy involves not only an expensive double summation over the grid points but also a divergent Coulomb term,  $1/r$ . In reciprocal space, the Hartree energy simply becomes

$$E_H = \frac{1}{V} \sum_{\mathbf{g} \neq 0} \left[ \frac{4\pi}{|\mathbf{g}|^2} + \tilde{\phi}^{(\text{screen})}(\mathbf{g}) \right] |n_{\mathbf{g}}|^2 + \frac{1}{V} \tilde{\phi}^{(\text{screen})}(0) |n_{0,0,0}|^2 \quad (24)$$

where  $n_{\mathbf{g}}$  is the Fourier component of the density corresponding to the reciprocal space vector  $\mathbf{g}$ , which is obtained by an FFT of the density in real-space, eq 19.  $V$  is the volume of the unit cell. The function  $\tilde{\phi}^{(\text{screen})}(\mathbf{g})$  is a “screening” function, derived in refs 44–46, that allows nonperiodic systems to be treated within a reciprocal-space approach.

**(c) Exchange-Correlation Energy.** It is often necessary to employ exchange-correlation (XC) functionals beyond the local density approximation. When the generalized gradient approximation (GGA) for the XC functional and the real-space method of White and Bird are used,<sup>47</sup>  $E_{\text{xc}}$  is given by a summation over the grid points as

$$E_{\text{xc}} = -\sum_{\alpha\beta\gamma} \frac{V}{N_{\alpha\beta\gamma}} n(\mathbf{r}_{\alpha\beta\gamma}) f_{\text{xc}}(n(\mathbf{r}_{\alpha\beta\gamma}), |\nabla n(\mathbf{r}_{\alpha\beta\gamma})|) \quad (25)$$

where  $f_{\text{xc}}$  is the exchange-correlation energy per particle. The gradient of the electron density at a DVR point,  $\mathbf{r}_{\alpha\beta\gamma}$ , can be derived analytically as

$$\nabla_x n(\mathbf{r}_{\alpha\beta\gamma}) = 2 \sum_i f_i \left[ \frac{C_{\alpha\beta\gamma}^i}{\omega_{\beta} \omega_{\gamma} \sqrt{\omega_{\alpha}}} \sum_{\alpha'} C_{\alpha'\beta\gamma}^i u'_{\alpha'}(x_{\alpha}) \right] \quad (26)$$

with analogous expressions for the  $y$  and  $z$  components of the gradient. Because a DVR function,  $u_{\alpha}(x)$ , is continuous and analytically defined as eq 6, its derivative,  $u'_{\alpha}(x)$ , can be computed at all DVR points along a given spatial direction and stored at the beginning of each simulation. To compute the forces on the DVR coefficients, the derivative of the density gradient with respect to the DVR coefficients must be computed.

For example, the derivative of the  $x$ -component of density gradient can be obtained from eq 26 as

$$\frac{\partial \nabla_x n(\mathbf{r}_{\alpha'\beta'\gamma'})}{\partial C_{\alpha\beta\gamma}^i} = 2f_i \left[ \frac{1}{\omega_{\beta}\omega_{\gamma}\sqrt{\omega_{\alpha}}} \sum_{\alpha''} C_{\alpha'\beta'\gamma'}^i u'_{\alpha''}(x_{\alpha}) \delta_{\alpha\alpha''} \delta_{\beta\beta''} \delta_{\gamma\gamma''} + \frac{C_{\alpha'\beta'\gamma'}^i}{\omega_{\beta}\omega_{\gamma}\sqrt{\omega_{\alpha}}} u'_{\alpha}(x_{\alpha'}) \right] \quad (27)$$

As with the kinetic energy, the summations can be efficiently computed by transposing the orbital coefficient array so that the summation is always performed over points that are contiguous in memory.

**(d) Local and Nonlocal Energies.** In the AIMD scheme, core electrons are usually replaced by atomic pseudopotentials ( $\hat{V}_{\text{pseud}}$ ), and the external energy,  $E_{\text{ext}}$ , in eq 15 is computed according to  $E_{\text{ext}} = \sum_i f_i \langle \psi_i | \hat{V}_{\text{pseud}} | \psi_i \rangle$ . Atomic pseudopotentials utilize a different radial potential for each angular momentum channel ( $l, m$ ) of each atom type and therefore they are generally nonlocal:

$$\hat{V}_{\text{pseud}} = \sum_J \sum_{I(J)} \sum_{l=0}^{\infty} \sum_{m=-l}^l v_{JI}(|\mathbf{r} - \mathbf{R}_{I(J)}|) |lm\rangle \langle lm| \quad (28)$$

where  $J$  runs over the number of atom types,  $I(J)$  denotes an index  $I$  that runs over the atoms of each type  $J$ , and  $|lm\rangle \langle lm|$  is a projection operator. The summation over  $l$  is truncated at  $\bar{l} - 1$  and, as a result, the pseudopotential operator is decomposed of into two parts, specifically, local and nonlocal terms given, respectively, by

$$\begin{aligned} \hat{V}_{\text{pseud}} &\approx \sum_J \sum_{I(J)} v_{JI}(|\mathbf{r} - \mathbf{R}_{I(J)}|) \hat{I} \\ &+ \sum_J \sum_{I(J)} \sum_{l=0}^{\bar{l}-1} \sum_{m=-l}^l \Delta v_{JI}(|\mathbf{r} - \mathbf{R}_{I(J)}|) |lm\rangle \langle lm| \\ &\equiv \hat{V}_{\text{pseud,loc}} + \hat{V}_{\text{pseud,NL}} \end{aligned} \quad (29)$$

where  $\Delta v_{JI}(r) = v_{JI}(r) - v_{\bar{J}I}(r)$  and  $\hat{I}$  is the identity operator. Like the Hartree term, the local part of the pseudopotential is computed in reciprocal space because the local potential includes a long-range term. In our previous work,<sup>30</sup> only the long-range part of the local potential was computed in reciprocal space and the short-range part was computed in real-space. Here, the entire local potential is computed in reciprocal space. Therefore, the local potential energy is computed by

$$\begin{aligned} E_{\text{loc}} &= \sum_J \sum_{I(J)} \int n(\mathbf{r}) v_{\text{loc},J}(|\mathbf{r} - \mathbf{R}_{I(J)}|) d\mathbf{r} \\ &= \frac{1}{V} \sum_J \sum_{I(J)} \sum_{\mathbf{g}} n_{\mathbf{g}}^* e^{-i\mathbf{g}\cdot\mathbf{R}_{I(J)}} [\tilde{v}_{\text{loc},J}(\mathbf{g}) - Z_{JI} \tilde{\phi}^{(\text{screen})}(\mathbf{g})] \end{aligned} \quad (30)$$

where  $\tilde{v}_{\text{loc},J}(\mathbf{g})$  is the FFT of the local potential  $v_{\text{loc},J}(r) \equiv v_{\bar{J}I}(r)$  and  $\mathbf{R}_{I(J)}$  is the location of atom  $I$  of type  $J$ . Here, again, the presence of the screening function allows for treatment of nonperiodic systems within the reciprocal-space framework. Because both the Hartree energy and local potential energy involve only the electron density (not the orbitals), we only need two FFTs to compute both terms. One FFT is needed to obtain  $n_{\mathbf{g}}$  and the other is needed to transform part of the potential back to real space for the calculation of the orbital forces. The contributions to the atomic forces from the local potential can

be computed in a straightforward manner using the reciprocal space energy expression.

The nonlocal part is further approximated and the fully separable form of Kleinman and Bylander<sup>48</sup> is used such that

$$\begin{aligned} E_{\text{NL}} &= \sum_i f_i \sum_J \sum_{I(J)} \int d\mathbf{r} d\mathbf{r}' \psi_i^*(\mathbf{r}') \psi_i(\mathbf{r}) \\ &\times \left[ \sum_{l=0}^{\bar{l}-1} \sum_{m=-l}^l \mathcal{N}_{JI} F_{Jlm}^*(\mathbf{r} - \mathbf{R}_{I(J)}) F_{Jlm}(\mathbf{r}' - \mathbf{R}_{I(J)}) \right] \\ &= \sum_i f_i \sum_J \sum_{I(J)} \sum_{lm} \mathcal{N}_{JI} Z_{iI(J)Jlm}^* Z_{iI(J)Jlm} \end{aligned} \quad (31)$$

where  $F_{Jlm}(\mathbf{r})$  is an angular momentum and atom type dependent function and  $\mathcal{N}_{JI}$  is a weight factor. The function  $F_{Jlm}(\mathbf{r})$  is proportional to the radial part of the pseudopotential  $\Delta v_{JI}(r)$  multiplied by a spherical harmonic  $Y_{lm}(\theta, \phi)$ . The quantity  $Z_{iI(J)Jlm}$  is defined by

$$Z_{iI(J)Jlm} = \int d\mathbf{r} F_{Jlm}(\mathbf{r} - \mathbf{R}_{I(J)}) \psi_i(\mathbf{r}) \quad (32)$$

In our previous work,<sup>30</sup> we evaluated the integral in eq 32 by a direct summation over the DVR grid points according to

$$\begin{aligned} Z_{iI(J)Jlm} &= \int \sum_{\alpha\beta\gamma} C_{\alpha\beta\gamma}^i \Phi_{\alpha\beta\gamma}(\mathbf{r}) F_{Jlm}(\mathbf{r} - \mathbf{R}_{I(J)}) d\mathbf{r} \\ &= \sum_{\alpha'\beta'\gamma'} \sum_{\alpha\beta\gamma} C_{\alpha\beta\gamma}^i \Phi_{\alpha\beta\gamma}(\mathbf{r}_{\alpha'\beta'\gamma'}) F_{Jlm}(\mathbf{r}_{\alpha'\beta'\gamma'} - \mathbf{R}_{I(J)}) \omega_{\alpha} \omega_{\beta} \omega_{\gamma} \\ &= \sum_{\alpha\beta\gamma} \sqrt{\omega_{\alpha} \omega_{\beta} \omega_{\gamma}} C_{\alpha\beta\gamma}^i F_{Jlm}(\mathbf{r}_{\alpha\beta\gamma} - \mathbf{R}_{I(J)}) \end{aligned} \quad (33)$$

To compute the forces on the atoms, the derivative of  $Z_{iI(J)Jlm}$  with respect to the atomic positions is needed:

$$\begin{aligned} \frac{\partial Z_{iI(J)Jlm}}{\partial \mathbf{R}_{I(J)}} &= \sum_{\alpha\beta\gamma} \sqrt{\omega_{\alpha} \omega_{\beta} \omega_{\gamma}} C_{\alpha\beta\gamma}^i \frac{\partial F_{Jlm}(\mathbf{r}_{\alpha\beta\gamma} - \mathbf{R}_{I(J)})}{\partial \mathbf{R}_{I(J)}} \\ &= - \sum_{\alpha\beta\gamma} \sqrt{\omega_{\alpha} \omega_{\beta} \omega_{\gamma}} C_{\alpha\beta\gamma}^i \left\{ \left[ \frac{\partial \Delta v_{JI}(r)}{\partial r} \right]_{r=|\mathbf{r}_{\alpha\beta\gamma} - \mathbf{R}_{I(J)}|} \right. \\ &\quad \left. Y_{lm}(\theta_{(\mathbf{r} - \mathbf{R}_{I(J)})}, \phi_{(\mathbf{r} - \mathbf{R}_{I(J)})}) + \Delta v_{JI}(|\mathbf{r} - \mathbf{R}_{I(J)}|) \frac{\partial Y_{lm}(\theta_{(\mathbf{r} - \mathbf{R}_{I(J)})}, \phi_{(\mathbf{r} - \mathbf{R}_{I(J)})})}{\partial |\mathbf{r} - \mathbf{R}_{I(J)}|} \right\} \frac{(\mathbf{r}_{\alpha\beta\gamma} - \mathbf{R}_{I(J)})}{|\mathbf{r} - \mathbf{R}_{I(J)}|} \end{aligned} \quad (34)$$

where  $(\theta_{(\mathbf{r} - \mathbf{R}_{I(J)})}, \phi_{(\mathbf{r} - \mathbf{R}_{I(J)})})$  are the polar angles associated with the vector  $\mathbf{r}_{\alpha\beta\gamma} - \mathbf{R}_{I(J)}$ . With the real-space expression of  $Z_{iI(J)Jlm}$ , the force on a DVR coefficient can be computed in a straightforward manner as

$$-\frac{\partial E_{\text{NL}}}{\partial C_{\alpha\beta\gamma}^i} = -2f_i \sum_J \sum_{I(J)} \sum_{lm} \mathcal{N}_{JI} F_{Jlm}(\mathbf{r}_{\alpha\beta\gamma} - \mathbf{R}_{I(J)}) Z_{iI(J)Jlm}^* \sqrt{\omega_{\alpha} \omega_{\beta} \omega_{\gamma}} \quad (35)$$

However, the real-space evaluation of eq 32, whose integrand consists of an atomic position-dependent function  $F_{Jlm}(\mathbf{r} - \mathbf{R}_{I(J)})$  and a field  $\psi_i(\mathbf{r})$ , is subject to an intrinsic problem called *aliasing*. If  $F_{Jlm}(\mathbf{r})$  contains Fourier components of frequency higher than the maximum frequency a given grid can support, the summation in eq 33 becomes dependent on the relative positions of the atoms with respect to the grid points. Therefore, the total energy is not translationally invariant. Note that the local potential energy (eq 30) contains a similar integrand, and

it also suffers from aliasing. However, the problem is much more serious for the nonlocal potential because it is short-ranged whereas the local potential has mostly long-range contributions.

The aliasing effect can be reduced by grid refinement techniques,<sup>49,50</sup> but such techniques increase the cost of nonlocal energy and force calculations substantially in the DVR framework. Instead, we take a more straightforward approach and remove the high-frequency components of the nonlocal potential by Fourier filtering at the beginning of the simulation.<sup>10,51</sup> Thus, the nonlocal pseudopotential functions  $\Delta v_{Jl}(r)$  are first transformed to reciprocal space by using a spherical Bessel transform:

$$\Delta \tilde{v}_{Jl}(g) = \sqrt{\frac{2}{\pi}} \int_0^\infty \Delta v_{Jl}(r) j_l(g r) r^2 dr \quad (36)$$

where  $j_l(r)$  is a spherical Bessel function of order  $l$ . Nonlocal pseudopotentials in reciprocal space are then multiplied by a switching function to damp out the high-frequency components. In the present work, a switching function of the form<sup>10</sup>

$$f(g) = e^{-\beta(g/g_{\text{cut}}-1)^2} \quad g > g_{\text{cut}} \quad (37)$$

$$f(g) = 1 \quad g \leq g_{\text{cut}} \quad (38)$$

was used, where  $g_{\text{cut}} = \alpha\pi/h$ . For the nonlocal pseudopotential of oxygen, we used  $\alpha = 0.85$  and  $\beta = 20$ . The modified pseudopotential functions are then transformed back to real-space by an inverse spherical bessel transform:

$$\Delta \tilde{v}_{Jl}(r) = \sqrt{\frac{2}{\pi}} \int_0^\infty \Delta \tilde{v}_{Jl}(g) f(g) j_l(g r) g^2 dg \quad (39)$$

Finally, the modified nonlocal pseudopotential functions  $\Delta \tilde{v}_{Jl}(r)$  are used in eq 33 and eq 35, to compute the nonlocal potential energy and force.

To demonstrate the effect of Fourier filtering, we monitored the electronic energy of single oxygen atom as its relative position with respect to grid points changes. Specifically, an oxygen atom is placed in a cubic periodic box of 8 Å and the electronic energies are computed as the atom is moved diagonally from one grid point to the next. In Figure 1a, we show the variation of the total electronic energy with and without the Fourier filtering. As shown in the figure, Fourier filtering reduces the grid dependence of energy more than an order of magnitude. For comparison, we also include a similar plot in Figure 1b obtained from the calculations with plane wave basis set of  $E_{\text{cut}}^{(\text{orb})} = 35$  Ry energy cutoff. This cutoff leads to the density FFT grid that has the same grid spacing as the DVR grid used in Figure 1a. The grid dependence of energy is negligible in plane wave calculations, and it is on the order of 0.0001 hartree for  $E_{\text{cut}}^{(\text{orb})} = 70$  Ry, a typical energy cutoff used in the simulation of liquid water.

As an illustration of the energy convergence of the DVR basis set approach in conjunction with the Fourier filtering, the energy of a water dimer in a cubic periodic box of length 15 bohr was computed as a function of the DVR grid spacing. The results are reported in Table 1. The calculations were carried out with the BLYP exchange-correlation functional<sup>31,32</sup> and the Troullier and Martin (TM) type<sup>52</sup> atomic pseudopotentials. The details of the algorithm to minimize the energy functional is described as section IV.A. From the table, it can be seen that the energy is converged to within 1 kcal/mol of the fully converged value with  $61^3$  DVR grid points whereas  $E_{\text{cut}}^{(\text{orb})} = 200$  Ry is needed for PW calculations to achieve the same level of accuracy.

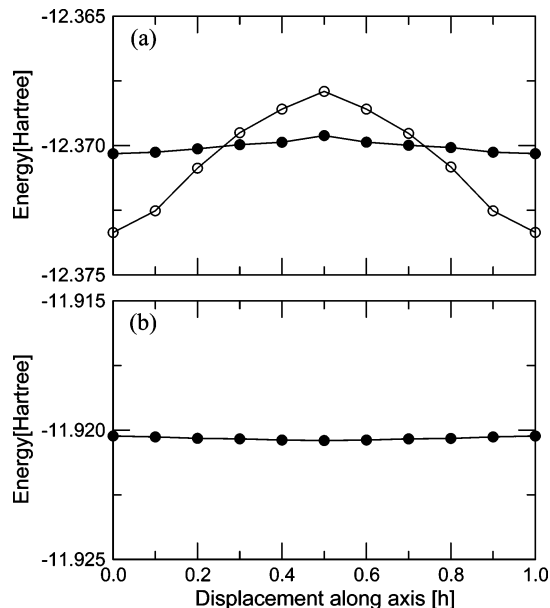


**Figure 1.** Variation of the electronic energy of single oxygen atom placed in a cubic periodic box of 8 Å as its position changes with respect to grid points. The unit of x-axis is the grid spacing,  $h$ . In (a), the results obtained for DVR basis ( $h = 0.25$  au) are shown with (closed circles) and without (open circles) the Fourier filtering. The results obtained for plane wave basis with  $E_{\text{cut}}^{(\text{orb})} = 35$  Ry energy cutoff are shown in (b). This energy cutoff leads to the density FFT grid with the same spacing as used in the DVR calculation.

**TABLE 1: Convergence of the Electronic Energy for a Water Dimer in a Cubic Periodic Box of 15 Bohr for the DVR and PW Basis Sets<sup>a</sup>**

grid size ( $E_{\text{cut}}^{(\text{orb})}$ )	$E(\text{DVR})$	$ \Delta E $	$E(\text{PW})$	$N_c(N_{\text{dens}})$	$ \Delta E $
$37^3$ (10)	-37.2903	40.7254	-33.1202	896 (7182)	2657.5027
$49^3$ (25)	-37.3576	1.5060	-35.5374	3562 (28139)	1140.6868
$61^3$ (35)	-37.3551	0.06275	-36.3767	5877 (47171)	614.0180
$73^3$ (50)	-37.3551	0.06275	-37.0060	10003 (80618)	219.1263
$81^3$ (80)	-37.3552	0	-37.3205	19660 (156211)	21.7745
$120^3$ (150)			-37.3533	52472 (418909)	1.1923
$144^3$ (200)			-37.3546	80618 (644880)	0.3765
$160^3$ (300)			-37.3552	146916 (1170999)	0

<sup>a</sup> The PW cutoff ( $E_{\text{cut}}^{(\text{orb})}$ ) given in parenthesis leads to the density FFT grid with the specified number of grid points. The energies are given in hartree and the energy difference ( $|\Delta E|$ ) measures the difference between the energy at each grid size and the converged energy in kcal/mol. Also given are the spherically truncated number of orbital ( $N_c$ ) and density ( $N_{\text{dens}}$ ) coefficients in PW calculations. Each atom that comprises the water dimer has the following Cartesian coordinates in Å: (2.6068, 3.9843, 4.1112), (5.5148, 4.0192, 3.8806) for oxygens and (2.2649, 3.2927, 3.5370), (2.2747, 4.8095, 3.7456), (5.9271, 3.8794, 4.7360), (4.5608, 3.9907, 4.0466) for hydrogens. Throughout the calculations, the atomic pseudopotentials of Troullier and Martin (TM) type<sup>52</sup> are employed in the Kleinman–Bylander<sup>48</sup> form for the nonlocal part of energy calculation with nonlocal  $S$  components on the oxygens only.

In the CPAIMD scheme, the nonlocal part of the pseudopotential calculation is a major bottleneck along with the orthogonalization step because both of these steps scale as  $\mathcal{O}(N^3)$ . This is clearly seen from eq 31 and eq 33 where each summation over  $i$ ,  $I(J)$  and the grid points scales as  $\mathcal{O}(N)$ . Although this poor scaling is not a serious issue for small systems, it quickly becomes dominant in CPAIMD simulations of larger systems. In real-space approaches, the scaling of the nonlocal part of the pseudopotential calculation can easily be reduced to  $\mathcal{O}(N^2)$  by using the fact that nonlocal pseudopotential functions  $\Delta v_{Jl}(r)$  are very short ranged. In other words, the

summation over the grid points in eq 33 can be restricted to the points inside of a sphere around each atom. Because the truncation radius ( $r_{\text{cut}}$ ) does not depend on the system size, the cost of computing all  $Z_{ij(l),lm}$  is reduced to  $\mathcal{O}(N^2)$ . However, when Fourier filtering is used, the transformed potential,  $\Delta\tilde{v}_{jl}(r)$ , does not strictly go to zero beyond  $r > r_{\text{cut}}$  and has a long oscillating tail. Although the magnitude of the tail is small, an arbitrary truncation causes a discontinuity in the forces, which may be problematic for long time simulations. Because the oscillating tail is not part of the original pseudopotential, a switching function can be applied to  $\Delta\tilde{v}_{jl}(r)$  to damp out the long range oscillation and make the potential rigorously go to zero. For a switching function in real-space, we used the form described in ref 53 for test calculations. For systems containing oxygen, the switching function might be taken to act, for example, between  $r = r_{\text{cut}} - 0.5$  au and  $r = r_{\text{cut}}$ . For the oxygen pseudopotential with the  $\alpha$  and  $\beta$  parameters specified above, a grid spacing of  $h = 0.25$  au combined with a truncation radius  $r_{\text{cut}} = 3.5$  au leads to an agreement in the total energy of 32 water system within 0.002 hartree (or  $6.3 \times 10^{-5}$  hartree per molecule) compared to the energy computed without the truncation. The reduction in computational overhead due to spherical truncation is significant for a 64-water system. Specifically, we achieved a factor of 4 saving for the nonlocal part of the calculation even with a relatively sparse grid spacing ( $h = 0.35$ ).

Although Fourier filtering is straightforward to implement and does not increase the computational cost, the ad hoc parameters,  $\alpha$  and  $\beta$ , must be chosen carefully. As an alternative, an interpolation scheme can be used to evaluate  $F_{Jlm}(\mathbf{r} - \mathbf{R}_{(l)})$  on the real-space grid. Recently, we introduced such a real-space scheme based on the Euler exponential spline interpolation for the nonlocal pseudopotential calculations in PW based CPAIMD simulations.<sup>54</sup> The method scales as  $\mathcal{O}(N^2)$  and can be adapted for the DVR based method as well. In the appendix, we briefly describe this approach as an alternative to overcome the aliasing effect.

## IV. Results

**A. Total Energy Calculation.** The total electronic energy of the system for a given configuration is computed by minimizing the energy functional using the conjugate gradient (CG) technique.<sup>55</sup> Previously, we applied a simple CG scheme without any preconditioning<sup>30</sup> to compute the ground state energies of bulk silicon and single water molecule. For small silicon systems, the convergence was reasonably fast for the purpose of investigating the efficiency of the DVR basis set. However, for larger systems, such as liquid water, the rate of convergence in the energy minimization is unacceptably slow if no preconditioner is used. In the CG method, the steepest descent vector that points to the direction of energy minimum is biased by the high-frequency components of wave functions. The role of the preconditioner is to offset these components so that the steepest decent direction represents the errors in the expansion coefficients more accurately. Multigrid approaches<sup>10,12</sup> normally used in real-space methods are based on similar arguments. In multigrid methods, multiple levels of grid density are used iteratively and the frequency components of the error that are best represented by the grid density of each level are removed.

In a plane wave basis, the Kohn–Sham Hamiltonian is diagonally dominant for the high  $\mathbf{g}$ -vector components of the basis set, and therefore, a simple diagonal preconditioning matrix is quite efficient. The Kohn–Sham Hamiltonian in DVR basis,

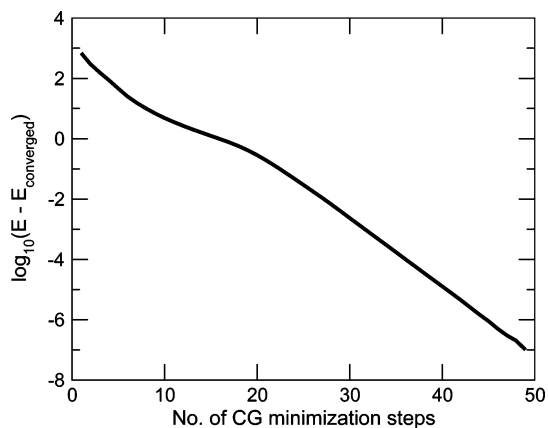


**Figure 2.** Convergence rate of the total energy minimization for a 32 water system in a cubic periodic box with 75 DVR basis functions per coordinate. The convergence rate,  $\log(E - E_{\text{converged}})$ , is plotted with respect to the conjugate gradient minimization steps. In this test, a preconditioner defined in eq 40 is used to accelerate the convergence.

however, is not diagonally dominant. Nevertheless, the behavior of the KS Hamiltonian in reciprocal space can be used to develop a preconditioner for the DVR basis. In the FBR of eq 9, the Hamiltonian matrix is diagonally dominant. Thus, we first transform the forces on the DVR coefficients into the FBR by using the inverse of the transformation matrix, eq 11 and divide the forces by the diagonal elements of the kinetic energy matrix. Therefore, each orbital force is multiplied in the FBR by

$$[\tilde{K}_{lmm'}^{l'm'n'}]^{-1} = (\tilde{K}_{ll}^x + \tilde{K}_{mm}^y + \tilde{K}_{nn}^z)^{-1} \delta_{ll'} \delta_{mm'} \delta_{nn'} \quad (40)$$

where

$$\tilde{K}_{nn}^a = \begin{cases} K_{nn}^a & |k_n| > k_{n_c} \\ K_{n_c n_c}^a & |k_n| \leq k_{n_c} \end{cases} \quad (41)$$

and  $K_{nn}^a$  is the kinetic energy matrix in FBR for the coordinate  $a$ . The resulting force vectors are then transformed back to the DVR basis by the transformation matrix.

The efficiency of the CG minimization scheme described above for a system of 32 water molecules in a cubic cell of 18.6226 bohr is shown in Figure 2. In the figure, the convergence rate,  $\log(E - E_{\text{converged}})$  is plotted. The calculation was performed using a grid spacing  $h = 0.25$  au, which is equivalent to an 160 Ry energy cutoff of a density expansion in a PW calculation (or a 40 Ry cutoff of the orbital expansion in a PW basis). The performance of the CG minimization shown in Figure 2 for a DVR basis set is similar to that which is usually achieved with a PW basis set.

To compare the total energy convergence with basis set size for DVR and PW basis sets, we show, in Figure 3, the total energy of 32 water system as a function of the number of grid points for the two basis sets. For the PW basis, the abscissa specifies the number of grid points used to represent the electronic density on the real-space grid. It can be clearly seen from the figure that the total energy is converged within  $2 \times 10^{-3}$  hartree ( $\sim 1.3$  kcal/mol) to the fully converged value ( $-313.876$  hartree) with  $75^3$  grid points ( $h = 0.25$  au as above) when a DVR basis set is used. For PW basis, at least 300Ry energy cutoff ( $N = 200$ ) is needed to obtain a comparable accuracy. At this cutoff, the number of (complex) orbital PW expansion coefficients on a spherically truncated grid is 281808, the number of (complex) density PW coefficients is 2250783, whereas the number of real-space grid points is 8 million

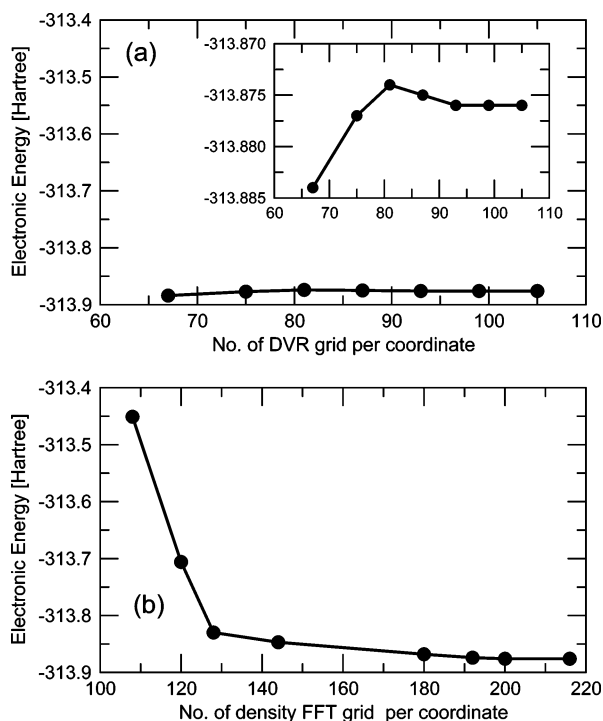


**Figure 3.** Total electronic energy of a 32 water system in a cubic periodic box obtained by preconditioned conjugate gradient minimizations of the energy functional using (a) DVR basis and (b) plane wave basis. The energy is plotted versus the number of DVR grid points per coordinate and number of density FFT grids per coordinate in the case of PW calculations. The orbital energy cutoff  $E_{\text{cut}}^{(\text{orb})} = 300$  Ry corresponds to  $200^3$  point density grid per coordinate and  $E_{\text{cut}}^{(\text{orb})} = 90$  Ry corresponds to  $120^3$  point density grid in (b). The inset in (a) shows the energy convergence on a finer  $y$ -scale.

compared to 421875 DVR grid points. Note that AIMD simulations of liquid water are usually performed with a PW basis set truncated at  $E_{\text{cut}}^{(\text{orb})} = 80$  Ry, where the total energy is  $\sim 0.43$  hartree (270 kcal/mol) away from the converged value. In CPAIMD simulations, the convergence of the atomic forces is more important than the energy convergence. In Figure 4 we show the convergence of the atomic force measure:

$$\bar{F} = \sqrt{\frac{1}{N} \sum_{i=1}^N |\mathbf{F}_i|^2} \quad (42)$$

The figure shows that improved convergence of the forces is also achieved within the DVR scheme. The efficiency of the DVR basis allows a CPAIMD simulation of liquid water in the complete basis set limit to be performed and the structure of the liquid within a given approximation to the exchange and correlation functional to be accurately determined

**B. AIMD Simulation of Liquid Water.** To provide an additional test of the accuracy and stability of the DVR based approach, we performed a CPAIMD simulation of liquid water. Liquid water is one of the most studied liquid phase systems using AIMD simulation techniques and has become a benchmark system to test and improve new algorithms. In particular, structural and dynamical information obtained from PW based CPAIMD simulations has provided valuable insight into the nature of hydrogen bonding and the unusually fast proton transport mechanisms in water.<sup>56,57</sup> As noted in the Introduction, a simulation of liquid water using real-space methodology has not yet been reported other than a short (0.14 ps) test run.<sup>26</sup> Therefore, to develop an efficient linear scaling CPAIMD

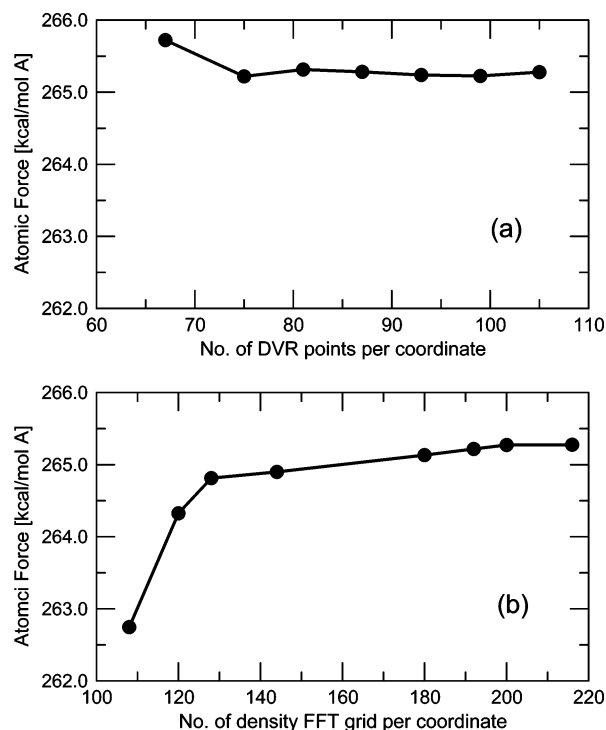


**Figure 4.** Atomic force measure, eq 42, in kcal/(mol·Å) corresponding to each point in Figure 3 for (a) DVR basis and (b) plane wave basis.

technique, it is important to assess the stability and accuracy of DVR based CPAIMD simulations of liquid water.

In the present work, an AIMD simulation based on the Car–Parrinello type adiabatic equations of motion is carried out for 32 water molecules in a cubic periodic box ( $L = 18.6226$  au) at the Gamma-point of the Brillouin zone. The electronic structure is represented within the Kohn–Sham (KS) formalism of density functional theory using the BLYP<sup>31,32</sup> exchange–correlation functional. The ability of this functional to describe accurately the structure of liquid water has been the subject of a recent controversy in the literature.<sup>33–37,39–41</sup> The Kohn–Sham orbitals are expanded in a DVR basis set corresponding to  $75^3$  grid points ( $h = 0.25$  au). As shown in the previous section, this grid setup leads to an energy convergence within  $2 \times 10^{-3}$  hartree. Core electrons are not treated explicitly but rather, the atomic pseudopotential of Troullier and Martin (TM) type<sup>52</sup> are employed in conjunction with the Fourier filtering scheme described in section II.

The initial configuration was taken from a separate CP run of 32 waters equilibrated for 5.2 ps at 300 K with a PW basis set cut off at 70 Ry using a Nosé–Hoover chain thermostat<sup>58</sup> on each degree of freedom. Following this, a run of 3.5 ps was performed with the same thermostating scheme using a slightly coarser grid of size  $h = 0.28$  au. Following this a run of 18 ps was performed using the  $h = 0.25$  au grid. Again, the temperature of the system was maintained at 300 K throughout the 18 ps DVR/CPAIMD simulation using a Nosé–Hoover chain thermostat<sup>58</sup> on each degree of freedom. The structural information of the system was obtained from the last 10 ps CPAIMD trajectory. The average temperature during the 10 ps production run is 298 K. As CP parameters, a time step of 0.05 fs along with a fictitious mass parameter  $\mu = 500$  au was employed. As shown below, this combination of fictitious mass and time step preserves the adiabatic separation between the ionic and electronic motions throughout the simulation. To reduce nuclear quantum effects, all protons were assigned the mass of deuterium. This mass assignment does not affect any

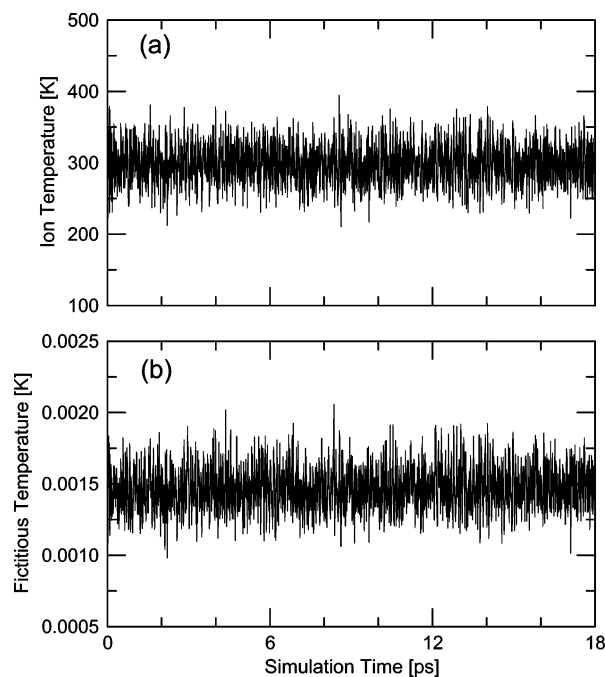


**Figure 5.** Instantaneous values of the (a) ionic temperature and (b) fictitious electronic temperature over an 18 ps DVR/CPAAMD simulation of 32 water system in a cubic periodic box ( $L = 18.6226$  au). 75 DVR functions were used for each coordinate. For the simulation parameters, a fictitious mass  $\mu = 500$  au and a time step of 0.05 fs are used along with a Nosé–Hoover chain thermostat coupled to each degree of freedom to maintain the ionic temperature at 300 K.

structural properties, such as radial distribution function. The calculation is performed with the DVR version of the PINY\_MD package.<sup>42</sup>

In Figure 5, the temperatures of the ionic and electronic degrees of freedom throughout the 18 ps constant temperature (NVT) simulation based on the DVR/CPAAMD scheme are plotted versus the simulation time. The adiabatic separation of these two temperatures is the fundamental requirement for a successful CPAAMD simulation. In particular, the stability of the temperature of fictitious electronic degrees of freedom is critical. As shown in the figure, excellent temperature control is maintained throughout the simulation, which indicates negligible exchange of energy between the ionic and electronic degrees of freedom. As pointed out by Kuo, et al.,<sup>36</sup> microcanonical ensemble (NVE) simulations following a few picoseconds of equilibration of liquid water system do not guarantee the equipartitioning of internal energy. A significant drift ( $> 10$  K<sup>36</sup>) in the ionic temperature was observed in NVE simulations regardless of the methods of simulation, both CPAAMD and BOAIMD simulations. In this sense, a constant temperature simulation with an efficient thermostating scheme is essential to determine accurately the structure of liquid water. As shown in Figure 5a, a Nosé–Hoover chain thermostat<sup>58</sup> coupled to each degree of freedom maintains the temperature without a drift and improves canonical sampling. The importance of the Nosé–Hoover chain thermostat as a means of controlling the temperature of *fictitious* degrees of freedom and performing longer simulations is also discussed in ref 36. However, as shown in Figure 5, the choice of time step and fictitious mass permit a long, stable simulation to be performed.

Figure 6 shows the oxygen–oxygen ( $g_{OO}(r)$ ), oxygen–hydrogen ( $g_{OH}(r)$ ) and hydrogen–hydrogen ( $g_{HH}(r)$ ) radial distribution functions (RDFs) obtained from a DVR/CPAAMD simulation. Each RDF was calculated using a bin size of 0.03 Å. The same bin size was used in recent CPAAMD studies of

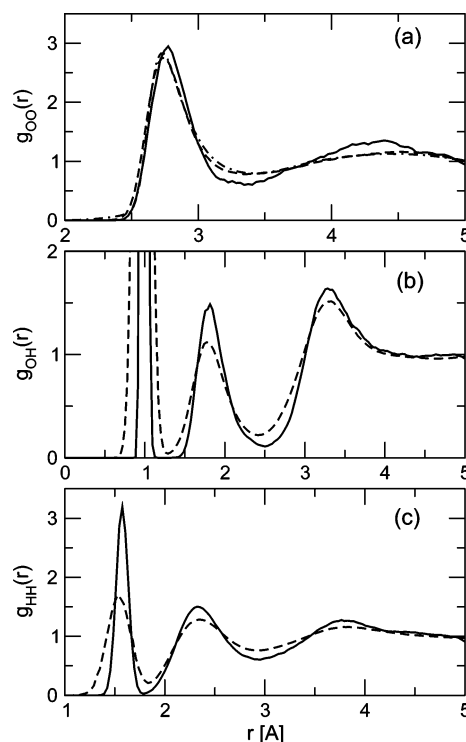


**Figure 6.** Radial distribution functions (RDF) obtained from an 18 ps DVR/CPAAMD simulation of 32 water molecules under the condition described in Figure 5 (Solid lines). Only the last 10 ps data are used to generate the RDFs. For comparison, experimental RDFs from the neutron scattering data of Soper and co-workers<sup>59,60</sup> (dashed lines) and, for OO, from the X-ray scattering data of Head-Gordon and co-workers<sup>61,62</sup> (dot–dashed line) are also plotted. Each panel represents RDF of (a) oxygen–oxygen (b) oxygen–hydrogen and (c) hydrogen–hydrogen, respectively. A bin size 0.03 Å is used for all three RDFs from the DVR/CPAAMD simulation.

liquid water.<sup>34,35</sup> The RDFs calculated using a bin size 0.02 Å were found indistinguishable from those reported in Figure 6. On the same plot, we show the experimental RDFs from the neutron scattering data of Soper and co-workers<sup>59,60</sup> and, for OO, we also show the X-ray scattering data of Head-Gordon and co-workers.<sup>61,62</sup> Overall, the agreement between the computed and experimental RDFs is quite good. The notable difference is a slight overstructuring of the second solvation shell in  $g_{OO}(r)$  compared to experiment. The height of the first peak in oxygen–oxygen RDF,  $g_{OO}^{\max}$ , is 2.95 and the location of maximum,  $r_{OO}^{\max}$ , is 2.77 Å. These are in good agreement with the results of recent CPAAMD studies of water<sup>36,40</sup> with the same types of exchange–correlation functional and pseudopotential, but with a PW expansion of the orbitals, which reported  $g_{OO}^{\max} = 3.0$  and  $r_{OO}^{\max} = 2.75$  Å at 314 K<sup>36</sup> and  $g_{OO}^{\max} \approx 3.1$  and  $r_{OO}^{\max} = 2.73$  Å at 300 K.<sup>40</sup> The coordination number was also computed by integrating  $g_{OO}(r)$  up to the first minimum. The coordination number obtained from Figure 6a is 4.2, which is close to the value for tetrahedral geometry. The oxygen–hydrogen RDF shown in Figure 6b has the first and second peaks located at 1.81 and 3.28 Å with the peak height 1.49 and 1.64 Å, respectively. These numbers also agree quite well with the results reported by Kuo et al.<sup>36</sup>

The structural parameters obtained recently by Grossman et al.<sup>34</sup> from CPAAMD simulations under microcanonical ensemble (NVE) condition with a Hamann type pseudopotential<sup>63</sup> appear to be overstructured compared to the present work and that of refs 36 and 40. These authors reported  $g_{OO}^{\max} = 3.60$  at 298 K for 32 water molecules with both BLYP and PBE<sup>64</sup> XC functionals. The differences in  $g_{OH}(r)$  and  $g_{HH}(r)$  between our

calculations and those by Grossman et al.<sup>34</sup> are much smaller, but noticeable. For instance, the height of the first intermolecular peak of  $g_{\text{OH}}(r)$  is 1.8 in ref 34, which is higher than the second peak. However, the opposite trend is found in the present study. The radial distribution functions recently reported by Vandevondele, et al.,<sup>38</sup> which employ Gaussian basis sets, different pseudopotentials, and NVE sampling, are also somewhat more structured than those obtained here. The PBE functional, on the other hand, seems to consistently generate overstructured liquid water, as reported by several groups.<sup>33,35,39</sup> Schwegler et al.<sup>35</sup> recently performed extensive simulations with 54 and 64 water molecules under NVE condition and found that the PBE functional generates significantly overstructured liquid water. For 54 water molecules, CPAIMD simulations yielded  $g_{\text{OO}}^{\text{max}} = 3.65$  at 296 K and  $g_{\text{OO}}^{\text{max}} = 3.21$  at 345 K. Similar behavior was also found in the BOAIMD study by Asthagiri et al.<sup>33</sup> who reported  $g_{\text{OO}}^{\text{max}} = 3.7$  at 337 K for the PBE functional. As in ref 34, the simulations of Asthagiri et al.<sup>33</sup> also employed NVE ensemble conditions.

More recently, Fernandez-Serra and Artacho<sup>37,41</sup> and Sit and Marzari<sup>39</sup> observed a sudden structural change after about 10 ps of AIMD with the BLYP and PBE functionals, respectively. As a result, a large difference in  $g_{\text{OO}}(r)$  before and after 10 ps was found. However, such behavior was not observed in the present work, likely because our initial configuration is already well equilibrated and effective sampling is ensured via the aforementioned thermostating protocol. To make sure that there is no systematic variation of the structural data during the simulation, we computed  $g_{\text{OO}}^{\text{max}}$  using blocks of 2 ps data. As pointed out by Grossman et al.,<sup>34</sup>  $g_{\text{OO}}^{\text{max}}$  has a rather short correlation time and 2 ps of data can provide an independent measure of  $g_{\text{OO}}^{\text{max}}$ . We found  $g_{\text{OO}}^{\text{max}} = 3.05, 3.19, 2.86, 2.83, 3.00$  during the production run (last 10 ps). Although five blocks of 2 ps data are not enough to draw a definite conclusion,  $g_{\text{OO}}^{\text{max}}$  values from our DVR/CPAIMD simulation seem to be well converged.

Overall, a long-term stability was achieved in the simulation of liquid water using the DVR/CPAIMD approach. This was shown in the excellent adiabatic separation between the ionic and electronic degrees of freedom. The energy conservation during the simulation, as measured by the quantity

$$\Delta E = \sum_{i=1}^{N_{\text{step}}} \left| \frac{E_i - E_0}{E_0} \right| \quad (43)$$

where  $E_i$  is the conserved energy at step  $i$ ,  $E_0$  is the initial energy, and  $N_{\text{step}}$  is the total number of MD steps performed, was on the order  $10^{-9}$ . These observations ensure the validity of force evaluation described in section III. As pointed out earlier, even a small error in the force calculations might ruin the stability of CPAIMD simulations. The structural information of liquid water obtained in this work from DVR/CPAIMD simulation is also in good agreement with the recent CPAIMD study by Kuo et al.<sup>36</sup> and of Mantz et al.<sup>40</sup> with the same types of functional and pseudopotential, but with a plane wave expansion of the orbitals. A more detailed analysis of the DVR water study will be reserved for a future publication.

## V. Conclusion and Future Work

In this paper, the algorithmic details for Car–Parrinello ab initio MD simulations using DVR basis sets were presented. Unlike typical plane wave based CPAIMD methods, only two FFTs are needed to compute the energy and coefficient forces.

We successfully performed a long term simulation of liquid water using the DVR approach and ensured the accuracy and stability of the DVR/CPAIMD scheme. With a relatively small number of grid points, we were able to run a simulation very close to the complete basis set limit with the DVR basis. The validity of the method was tested by comparing the structural information derived from a DVR/CPAIMD run to the existing data obtained from PW/CPAIMD calculations. To the best of our knowledge, this is the first successful simulation of liquid water using a real-space approach that generated accurate structural information.

The success of the present liquid water simulations provides us a unique opportunity to further investigate the structural and dynamical properties of the liquid water and aqueous solutions. As mentioned in section IV, the properties of liquid water obtained from numerous groups using AIMD techniques do not always agree with each other,<sup>33–37,39–41</sup> especially at ambient conditions. However, as pointed out in refs 36 and 38, a likely source of the difference is the nonergodic behavior at lower temperature, in particular under NVE conditions. Therefore, the use of a thermostating scheme is clearly important for ensuring proper generation of static equilibrium properties. However, there are many other factors to be taken into account to investigate the effect of equilibration. For instance, AIMD studies have used a variety of basis sets with varying degrees of total energy convergence, but the effect of energy convergence on the properties of liquid water for a given functional is not clear. An advantage of using the DVR/CPAIMD scheme over the PW/CPAIMD method is the ability to reach the complete basis-set limit.

Another important implication of the success of the DVR/CPAIMD scheme for liquid water is that the method can be used to develop a linear scaling AIMD simulation technique. Recently, Fattebert and Gygi proposed a linear scaling scheme based on the BOAIMD method.<sup>26</sup> Although they did not explicitly show the scaling of their method, they were able to run dynamics with a localization constraint for a short period of time (1 ps for deuterium and 0.14 ps for 64 water). Because the merits of BOAIMD vs CPAIMD remain unclear,<sup>3,27</sup> it is useful to devise a linear scaling method based on the CPAIMD scheme. We are currently developing such a method based on “on-the-fly” localization of the occupied orbitals. In particular, we are undertaking theoretical groundwork using nonorthogonal orbitals,<sup>16,65,66</sup> which provide greater degree of localization compared to the orthogonal ones.

**Acknowledgment.** We gratefully acknowledge Dr. Dawn A. Yarne for helpful discussions. This work was supported by NSF CHE-0121375 and NSF CHE-0310107.

## Appendix A: Euler Exponential Spline Interpolation for the Nonlocal Pseudopotential Calculation

In this appendix, we briefly describe an alternative expression for the nonlocal energy based on the Euler exponential spline interpolation.<sup>67</sup> More details of the algorithm can be found elsewhere.<sup>54</sup> We first express the function  $F_{Jlm}(\mathbf{r} - \mathbf{R}_{l(j)})$  in terms of a Fourier series as

$$F_{Jlm}(\mathbf{r} - \mathbf{R}_{l(j)}) = \frac{1}{V} \sum_{\mathbf{g}} \tilde{F}_{Jlm}(\mathbf{g}) e^{i\mathbf{g} \cdot (\mathbf{r} - \mathbf{R}_{l(j)})} \quad (\text{A1})$$

where  $\tilde{F}_{Jlm}(\mathbf{g})$  is not an FFT of  $F_{Jlm}(\mathbf{r})$  but an exact Fourier transform given as

$$\tilde{F}_{Jlm}(\mathbf{g}) = 4\pi Y_{lm}(\theta_{\mathbf{g}}, \phi_{\mathbf{g}}) \int_0^{\infty} r^2 j_l(gr) v_{jl}(r) \phi_{jl}(r) dr \quad (\text{A2})$$

where  $\phi_{ll}(r)$  is the ground state  $l$ -channel radial eigenfunction. Next, an Euler exponential spline (EES) interpolation to the atomic structure factor in eq A1 is introduced to give

$$e^{i\mathbf{g}\cdot\mathbf{R}_{l(j)}} \approx \prod_{a=x,y,z} d_p(\hat{g}_a, N_a) \sum_{\hat{s}_a=-\infty}^{\infty} M_p(u_{l,a} - \hat{s}_a) e^{2\pi i \hat{g}_a \hat{s}_a / N_a} \quad (\text{A3})$$

where  $\hat{g}_a$  and  $\hat{s}_a$  are integers,  $N_a$  is the number of grid points along the  $a$  direction,  $u_{l,a}$  is the fractional coordinate (real) of atom  $l$  for the coordinate  $a$  ( $0 \leq u_{l,a} < N_a$ ),  $M_p(u)$  is a Cardinal  $B$ -spline function,<sup>67</sup> and  $d_p(\hat{g}_a, N_a)$  is the corresponding weight.  $B$ -spline functions are continuously differentiable and have finite support. Substituting eq A3 into eq A1, we obtain the interpolation formula on the grid points,

$$\begin{aligned} F_{Jlm}(\mathbf{r}' - \mathbf{R}_{l(j)}) &\approx F_{Jlm}^{(EES)}(\mathbf{h}\mathbf{s}' - \mathbf{R}_{l(j)}) \\ &= \sum_{\hat{s}} \left[ \prod_a M_p(u_{l,a} + \hat{s}_a - \hat{s}'_a) \right] \chi_{Jlm}(\mathbf{s}) \\ \chi_{Jlm}(\mathbf{s}) &= \sum_{\hat{\mathbf{g}}} \left[ \prod_a e^{2\pi i \hat{g}_a \hat{s}_a / N_a} d_p(\hat{g}_a, N_a) \right] \tilde{F}_{Jlm}(\mathbf{g}) \quad (\text{A4}) \end{aligned}$$

where  $\mathbf{h}$  is the cell matrix and  $\hat{s}'_a$  is the fractional coordinate (integer) for the grid point  $\mathbf{r}' = \mathbf{h}\mathbf{s}'$ . Note that  $\chi_{Jlm}(\mathbf{s})$  does not depend on the atomic positions and therefore it needs to be evaluated once. Because the Fourier transform  $\tilde{F}_{Jlm}(\mathbf{g})$  is not truncated at  $2\hat{\mathbf{g}}_{\max} = (N_a, N_b, N_c)$ , the projector can vary on length scales smaller than  $s_\alpha = N_\alpha^{-1}$ . Letting  $\hat{\mathbf{g}} \rightarrow \hat{\mathbf{g}} + \hat{\mathbf{G}}$  where  $-N_\alpha/2 < \hat{g}_a \leq N_\alpha/2$  and  $\hat{\mathbf{G}}_a = M_\alpha N_\alpha$ ,

$$\chi_{Jlm}(\mathbf{s}) = \sum_{\hat{\mathbf{g}}} \left[ \sum_{\mathbf{G}} \tilde{F}_{Jlm}(\mathbf{g} + \mathbf{G}) \right] \left[ \prod_\alpha e^{2\pi i \hat{g}_\alpha \hat{s}_\alpha} d_p(\hat{g}_\alpha, N_\alpha) \right] \quad (\text{A5})$$

because  $d_p(\hat{g}_\alpha, N_\alpha)$  and the complex exponentials are periodic functions of  $\mathbf{G}$ . The functions,  $\tilde{F}_{Jlm}(\mathbf{g} + \mathbf{G})$ , go to zero exponentially quickly at large argument,  $|\mathbf{g} + \mathbf{G}|$  and convergence of the  $\mathbf{G}$  sum is rapid.

The length of summation over  $\hat{s}$  depends on the order of interpolation,  $p$ , and does not increase as the system size grows. In practice, both  $\tilde{F}_{Jlm}(\mathbf{g})$  and  $\chi_{Jlm}(\mathbf{s})$  are computed and stored at the beginning of simulation. Then, the sum over the integers,  $\hat{s}_a$ , for each atom is performed as in eq A4 for all points  $\mathbf{r}'$  around each atom type within the radial cutoff. Finally,  $Z_{i(l)Jlm}$  is computed as defined in eq 33 by summing over the spherically truncated grids around each atom. Because the truncation radius does not increase with the system size, the computational cost of computing  $Z_{i(l)Jlm}$  for a given state ( $i$ ) and atom ( $l$ ) becomes system size independent and the overall cost of computing nonlocal energy and force scales as  $\mathcal{O}(N^2)$ .

The forces on the atoms can also be computed in an efficient and straightforward manner. As shown in eq 34, evaluation of atomic forces requires the derivative of  $F_{Jlm}(\mathbf{r}' - \mathbf{R}_{l(j)})$  with respect to the atomic positions. However, within the Euler spline interpolation formalism, the only term that depends on the atomic position is the  $B$ -spline function. Therefore, the expression for the derivative of  $F_{Jlm}(\mathbf{r}' - \mathbf{R}_{l(j)})$  is identical to eq A4 with  $M_p$  replaced by its derivative, which can be computed easily through the recursion relation,

$$\frac{d}{du} M_p(u) = M_{p-1}(u) - M_{p-1}(u-1) \quad (\text{A6})$$

## References and Notes

(1) Payne, M. C.; King-Smith, R. D.; Lin, J.-S.; Joannopoulos, J. D. *Rev. Mod. Phys.* **1992**, *64*, 1045.

- (2) Parrinello, M. *Solid State Commun.* **1997**, *102*, 107.  
(3) Marx, D.; Hutter, J. In *Modern Methods and Algorithms of Quantum Chemistry, NIC series*; Grotendorst, J., Ed.; John von Neuman Institut für Computing, Forschungszentrum: Jülich, 2000; Vol. 1, pp 301–449.  
(4) Tuckerman, M. E. *J. Phys. Condens. Matter* **2002**, *14*, R1297.  
(5) Car, R.; Parrinello, M. *Phys. Rev. Lett.* **1985**, *55*, 2471.  
(6) Hartke, B.; Carter, E. A. *Chem. Phys. Lett.* **1992**, *189*, 358.  
(7) Schlegel, H. B.; et al. *J. Chem. Phys.* **2001**, *114*, 9758.  
(8) Lippert, G.; Hutter, J.; Parrinello, M. *Mol. Phys.* **1997**, *92*, 477.  
(9) Chelikowsky, J. R.; Jing, X.; Wu, K.; Saad, Y. *Phys. Rev. B* **1996**, *53*, 12071.  
(10) Briggs, E. L.; Sullivan, D. J.; Bernholc, J. *Phys. Rev. B* **1996**, *54*, 14362.  
(11) Goedecker, S. *Rev. Mod. Phys.* **1999**, *71*, 1085.  
(12) Beck, T. L. *Rev. Mod. Phys.* **2000**, *72*, 1041.  
(13) Varga, K.; Zhang, Z.; Pantelides, S. T. *Phys. Rev. Lett.* **2004**, *93*, 176403.  
(14) Yang, W. *Phys. Rev. Lett.* **1991**, *66*, 1438.  
(15) Li, X.-P.; Nunes, R. W.; Vanderbilt, D. *Phys. Rev. B* **1993**, *47*, 10891.  
(16) Mauri, F.; Galli, G.; Car, R. *Phys. Rev. B* **1993**, *47*, 9973.  
(17) Ordejón, P.; Drabold, D. A.; Martin, R. M.; Grumbach, M. P. *Phys. Rev. B* **1995**, *51*, 1456.  
(18) Hernández, E.; Gillan, M. J.; Goringe, C. M. *Phys. Rev. B* **1996**, *53*, 7147.  
(19) Chelikowsky, J. R.; Troullier, N.; Saad, Y. *Phys. Rev. Lett.* **1994**, *72*, 1240.  
(20) Tsuchida, E.; Tsukada, M. *Phys. Rev. B* **1995**, *52*, 1995.  
(21) Skylaris, C.-K.; Haynes, P. D.; Mostofi, A. A.; Payne, M. C. *J. Chem. Phys.* **2005**, *122*, 084119.  
(22) Brandt, A.; McCormick, S. F.; Ruge, J. W. *SIAM J. Sci. Stat. Comput.* **1983**, *4*, 244.  
(23) Hackbusch, W. *Multi-Grid Methods and Applications*; Springer-Verlag: Berlin, 1985.  
(24) Alemany, M. M. G.; Jain, M.; Kronik, L.; Chelikowsky, J. R. *Phys. Rev. B* **2004**, *69*, 075101.  
(25) Schmid, R. *J. Comput. Chem.* **2004**, *25*, 799.  
(26) Fattebert, J.-L.; Gygi, F. *Comput. Phys. Comm.* **2004**, *162*, 24.  
(27) Tangney, P. *J. Chem. Phys.* **2006**, *124*, 044111.  
(28) Light, J. C.; Hamilton, I. P.; Lill, J. V. *J. Chem. Phys.* **1985**, *82*, 1400.  
(29) Light, J. C.; Carrington, T. *Adv. Chem. Phys.* **2000**, *114*, 263.  
(30) Liu, Y.; Yarne, D. A.; Tuckerman, M. E. *Phys. Rev. B* **2003**, *68*, 125110.  
(31) Becke, A. D. *Phys. Rev. A* **1988**, *38*, 3098.  
(32) Lee, C.; Yang, W.; Parr, R. G. *Phys. Rev. B* **1988**, *37*, 785.  
(33) Asthagiri, D.; Pratt, L. R.; Kress, J. D. *Phys. Rev. E* **2003**, *68*, 041505.  
(34) Grossman, J. G.; et al. *J. Chem. Phys.* **2004**, *120*, 300.  
(35) Schwegler, E.; Grossman, J. C.; Gygi, F.; Galli, G. *J. Chem. Phys.* **2004**, *121*, 5400.  
(36) Kuo, I. W.; et al. *J. Phys. Chem. B* **2004**, *108*, 12990.  
(37) Fernández-Serra, M. V.; Artacho, E. *J. Chem. Phys.* **2004**, *121*, 11136.  
(38) VandeVondele, J.; et al. *J. Chem. Phys.* **2005**, *122*, 014515.  
(39) Sit, P. H.-L.; Marzari, N. *J. Chem. Phys.* **2005**, *122*, 204510.  
(40) Mantz, Y. A.; Chen, B.; Martyna, G. J. *J. Chem. Phys. Lett.* **2005**, *405*, 294. Mantz, Y. A.; Chen, B.; Martyna, J. G. *J. Phys. Chem. B* **2006**, *110*, 3540.  
(41) Fernández-Serra, M. V.; Artacho, E. *Mol. Sim.* **2005**, *31*, 361.  
(42) Tuckerman, M. E.; et al. *Comput. Phys. Comm.* **2000**, *128*, 333.  
(43) Colbert, D. T.; Miller, W. H. *J. Chem. Phys.* **1992**, *96*, 1982.  
(44) Martyna, G. J.; Tuckerman, M. E. *J. Chem. Phys.* **1992**, *110*, 2810.  
(45) Minary, P.; Tuckerman, M. E.; Pihakari, K. A.; Martyna, G. J. *J. Chem. Phys.* **2002**, *116*, 5351.  
(46) Minary, P.; et al. *J. Chem. Phys.* **2004**, *121*, 11949.  
(47) White, J. A.; Bird, D. M. *Phys. Rev. B* **1994**, *50*, 4954.  
(48) Kleinman, L.; Bylander, D. M. *Phys. Rev. Lett.* **1982**, *48*, 1452.  
(49) Beck, T. L. *J. Comput. Chem.* **1999**, *20*, 1731.  
(50) Ono, T.; Hirose, K. *Phys. Rev. Lett.* **1999**, *82*, 5016.  
(51) Briggs, E. L.; Sullivan, D. J.; Bernholc, J. *Phys. Rev. B* **1995**, *52*, R5471.  
(52) Troullier, N.; Martins, J. L. *Phys. Rev. B* **1991**, *43*, 1993.  
(53) Tuckerman, M. E.; Berne, B. J.; Martyna, G. J. *J. Chem. Phys.* **1991**, *94*, 6811. Watanabe, M.; Reinhardt, W. P. *Phys. Rev. Lett.* **1990**, *65*, 3301.  
(54) Lee, H.-S.; Tuckerman, M. E.; Martyna, G. J. *ChemPhysChem* **2005**, *6*, 1827.  
(55) Press, W. H.; Teukolsky, S. A.; Vetterling, W. T.; Flannery, B. P. *Numerical Recipes*; Cambridge University Press: Cambridge, U.K., 1989.

- (56) Tuckerman, M. E.; Laasonen, K.; Sprik, M.; Parrinello, M. *J. Chem. Phys.* **1995**, *103*, 150.
- (57) Marx, D.; Tuckerman, M. E.; Hutter, J.; Parrinello, M. *Nature* **1999**, *397*, 601.
- (58) Martyna, G. J.; Klein, M. L.; Tuckerman, M. E. *J. Chem. Phys.* **1992**, *97*, 2635.
- (59) Soper, A. K.; Bruni, F.; Ricci, M. A. *J. Chem. Phys.* **1997**, *106*, 247.
- (60) Soper, A. K. *Chem. Phys.* **2000**, *258*, 121.
- (61) Hura, G.; Sorenson, J. M.; Glaeser, R. M.; Head-Gordon, T. *J. Chem. Phys.* **2000**, *113*, 9140.
- (62) Hura, G.; Sorenson, J. M.; Glaeser, R. M.; Head-Gordon, T. *J. Chem. Phys.* **2000**, *113*, 9148.
- (63) Hamann, D. R. *Phys. Rev. B* **1989**, *40*, 2980.
- (64) Perdew, J. P.; Burke, K.; Ernzerhof, M. *Phys. Rev. Lett.* **1996**, *77*, 3865.
- (65) Liu, S.; Perez-Jorda, J. M.; Yang, W. *J. Chem. Phys.* **2000**, *112*, 1634.
- (66) Fattebert, J.-L.; Bernholc, J. *Phys. Rev. B* **2000**, *62*, 1713.
- (67) Essmann, U.; et al. *J. Chem. Phys.* **1995**, *103*, 8577.
- (68) Vadali, R. V.; Shi, Y.; Kumar, S.; Kale, L. V.; Tuckerman, M. E.; Martyna, G. J. *J. Comp. Chem.* **2004**, *25*, 2006.